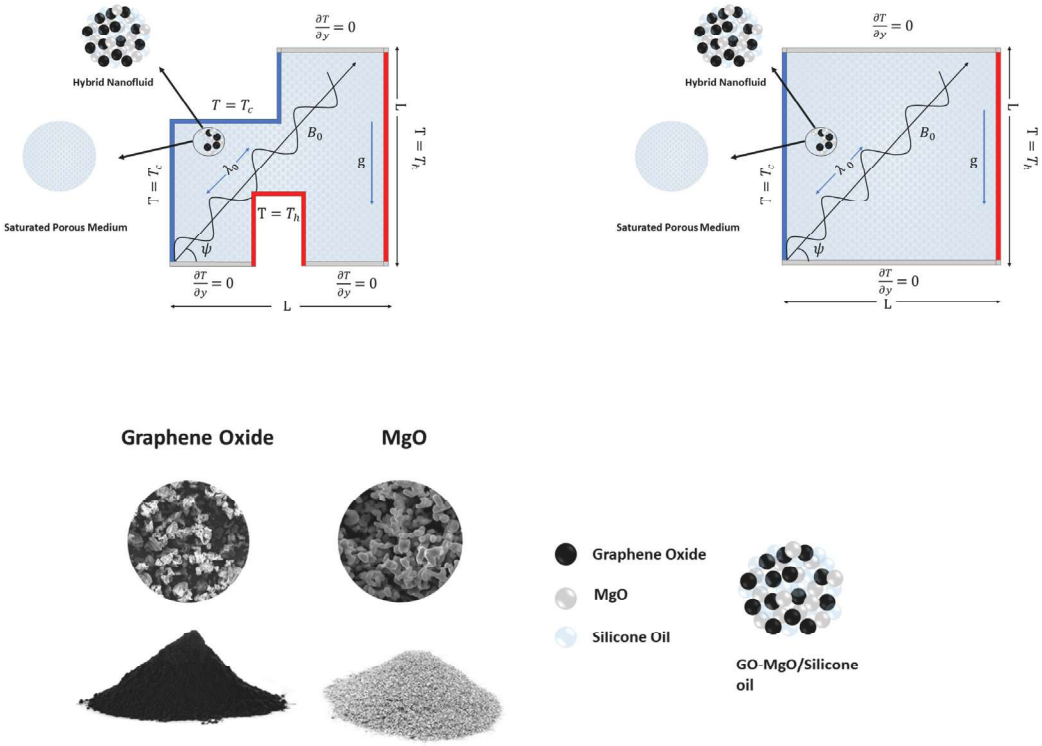

Fig. 1. Graphical representation of the present model.

Table 1
Thermophysical properties of GO, MgO, and silicone oil [47–53].

Physical properties	Graphene oxide	Magnesium oxide	Silicone oil
Density $\rho\left(\frac{kg}{m^3}\right)$	1800	3560	818
Specific heat capacity $C_p\left(\frac{J}{kg\ K}\right)$	717	955	1966
Thermal conductivity $k\left(\frac{W}{m\ K}\right)$	5000	45	0.1
Thermal expansion $\beta\ \times 10^{-5}\left(\frac{1}{K}\right)$	28.4	1.05	134
Electrical conductivity $\sigma\ \left(\frac{S}{m}\right)$	6.3×10^{7}	5.392×10^{-7}	1.5×10^{-6}

$$\begin{cases} \frac{\partial T}{\partial y} = 0 \quad \text{at } y = 0 \text{ for } 0 \le x \le 0.4L, \\ T = T_h \quad \text{at } y = 0.3L \text{ for } 0.4L \le x \le 0.6L, \\ \frac{\partial T}{\partial y} = 0 \quad \text{at } y = 0 \text{ for } 0.6L \le x \le L, \end{cases}$$

For bottom cut portion of h-shape cavity:

$$T = T_h \quad \text{at } x = 0.4 \ \&\ x = 0.6 \text{ for } 0 \le y \le 0.3L,$$

For left wall of h-shape cavity: $\begin{cases} T = T_c \quad \text{at } x = 0 \text{ for } 0 \le y \le 0.6L, \\ T = T_c \quad \text{at } x = 0.5L \text{ for } 0.6L \le y \le L, \end{cases}$

For right wall of h-shape cavity: $T = T_h$ at $x = L$ for $0 \le y \le L$,

For top wall of square cavity: $\frac{\partial T}{\partial y} = 0$ at $y = L$ for $0 \le x \le L$,

For bottom wall of square cavity: $\frac{\partial T}{\partial y} = 0$ at $y = 0$ for $0 \le x \le L$,

For left wall of square cavity: $T = T_c$ at $x = 0$ for $0 \le y \le L$,

For right wall of square cavity: $T = T_h$ at $x = L$ for $0 \le y \le L$,

Nanoparticles are suspended in the base fluid to increase the thermophysical properties of the base fluid. The thermophysical properties of the hybrid nanofluid are shown below [54–56].

Thermal conductivity:

$$k_{hnf} = k_{nf}\left[\frac{k_{s2} + (m-1)k_{nf} - (m-1)\phi_{s2}(k_{nf} - k_{s2})}{k_{s2} + (m-1)k_{nf} + \phi_{s2}(k_{nf} - k_{s2})}\right],$$

where,

$$k_{nf} = k_{bf}\left[\frac{k_{s1} + (m-1)k_{bf} - (m-1)\phi_{s1}(k_{bf} - k_{s1})}{k_{s1} + (m-1)k_{bf} + \phi_{s1}(k_{bf} - k_{s1})}\right],$$

Density:

$$\rho_{hnf} = \rho_{bf}\left[\phi_{s2}\frac{\rho_{s2}}{\rho_{bf}} + (1-\phi_{s2})\left(1 - \phi_{s1} + \phi_{s1}\frac{\rho_{s1}}{\rho_{bf}}\right)\right],$$

Dynamic viscosity:

$$\mu_{hnf} = \mu_{bf}\left[\frac{1}{(1-\phi_{s1})^{2.5}(1-\phi_{s2})^{2.5}}\right],$$

Thermal expansion:

$$(\rho\beta)_{hnf} = (\rho\beta)_{bf} \times \left[\phi_{s2}\frac{(\rho\beta)_{s2}}{(\rho\beta)_{bf}} + (1-\phi_{s2})\left(1 - \phi_{s1} + \phi_{s1}\frac{(\rho\beta)_{s1}}{(\rho\beta)_{bf}}\right)\right],$$

Specific heat capacity:

$$(\rho C_p)_{hnf} = (\rho C_p)_{bf} \times \left[\phi_{s2}\frac{(\rho C_p)_{s2}}{(\rho C_p)_{bf}} + (1-\phi_{s2})\left(1 - \phi_{s1} + \phi_{s1}\frac{(\rho C_p)_{s1}}{(\rho C_p)_{bf}}\right)\right],$$

Electrical conductivity:

$$\sigma_{hnf} = \sigma_{nf}\left[\frac{\sigma_{s2} + 2\sigma_{nf} - 2\phi_{s2}(\sigma_{nf} - \sigma_{s2})}{\sigma_{s2} + 2\sigma_{nf} + \phi_{s2}(\sigma_{nf} - \sigma_{s2})}\right],$$

where,

$$\sigma_{nf} = \sigma_{bf}\left[\frac{\sigma_{s1}+2\sigma_{bf} - 2\phi_{s1}(\sigma_{bf}-\sigma_{s1})}{\sigma_{s1}+2\sigma_{bf} + \phi_{s1}(\sigma_{bf}-\sigma_{s1})}\right],$$

Thermal Diffusivity:

$$\alpha_{hnf} = \frac{k_{hnf}}{(\rho C_p)_{hnf}}.$$

The radiative flux is being modeled using the Rosseland diffusion approximation [57]:

$$q_{rx} = -\frac{4\sigma^*}{3\beta_r}\frac{\partial T^4}{\partial x},\ q_{ry} = -\frac{4\sigma^*}{3\beta_r}\frac{\partial T^4}{\partial y},\ q = (q_{ry}, q_{ry}, 0). \tag{5}$$

The Taylor series is utilized to extend T^4 in measures of the low wall temperature T_c and omitting higher-order components, yielding:

$$T^4 \approx 4TT_c{}^3 - 3T_c{}^4. \tag{6}$$

Variables used to non-dimensionalize the governing equations:

$$X = \frac{x}{L}, Y = \frac{y}{L},\ t = \frac{t^*\alpha_{bf}}{L^2},\ U = \frac{uL}{\alpha_{bf}},\ V = \frac{vL}{\alpha_{bf}},\ P = \frac{pL^2}{\rho_{bf}\alpha_{bf}{}^2},$$
$$\theta = \frac{T-T_c}{T_h-T_c},\ \lambda = \frac{\lambda_0}{L}. \tag{7}$$

The following dimensionless equations are obtained from Eqs. (1)–(4) by combining Eqs. (5)–(7):

$$\frac{\partial U}{\partial X} + \frac{\partial V}{\partial Y} = 0, \tag{8}$$

$$\frac{1}{Pr}\frac{\rho_{hnf}}{\rho_{bf}}\left(\frac{\partial U}{\partial t} + U\frac{\partial U}{\partial X} + V\frac{\partial U}{\partial Y}\right) = -\frac{1}{Pr}\frac{\partial P}{\partial X} + \frac{\mu_{hnf}}{\mu_{bf}}\left(\frac{\partial^2 U}{\partial X^2} + \frac{\partial^2 U}{\partial Y^2}\right) - \frac{\mu_{hnf}}{\mu_{bf}}\frac{U}{Da} + \frac{\sigma_{hnf}}{\sigma_{bf}}Ha^2\sin^2\left(\frac{2\pi}{\lambda}(X cos\psi + Y sin\psi)\right) \times \left(V sin\psi cos\psi - U sin^2\psi\right), \tag{9}$$

$$\frac{1}{Pr}\frac{\rho_{hnf}}{\rho_{bf}}\left(\frac{\partial V}{\partial t} + U\frac{\partial V}{\partial X} + V\frac{\partial V}{\partial Y}\right) = -\frac{1}{Pr}\frac{\partial P}{\partial Y} + \frac{\mu_{hnf}}{\mu_{bf}}\left(\frac{\partial^2 V}{\partial X^2} + \frac{\partial^2 V}{\partial Y^2}\right) - \frac{\mu_{hnf}}{\mu_{bf}}\frac{V}{Da} + \frac{(\rho\beta)_{hnf}}{(\rho\beta)_{bf}}Ra\,\theta + \frac{\sigma_{hnf}}{\sigma_{bf}}Ha^2\sin^2\left(\frac{2\pi}{\lambda}(X cos\psi + Y sin\psi)\right) \times \left(U sin\psi cos\psi - V cos^2\psi\right), \tag{10}$$

$$\left(\frac{\partial\theta}{\partial t} + U\frac{\partial\theta}{\partial X} + V\frac{\partial\theta}{\partial Y}\right) = \frac{(\rho C_p)_{bf}}{(\rho C_p)_{hnf}}\left(\frac{k_{hnf}}{k_{bf}} + \frac{4}{3}Rd\right)\left(\frac{\partial^2\theta}{\partial X^2} + \frac{\partial^2\theta}{\partial Y^2}\right) + \left(\frac{(\rho C_p)_{bf}}{(\rho C_p)_{hnf}}\right)Q\theta. \tag{11}$$

where, heat source/sink (Q), Prandtl number (Pr), Darcy number (Da), thermal radiation (Rd), Hartmann number (Ha), Rayleigh number (Ra) are the pertinent parameters of this study:

$$Q = \frac{Q_H L^2}{\alpha_{bf}(\rho C_p)_{bf}},\ Pr = \frac{\nu_{bf}}{\alpha_{bf}},\ Da = \frac{K}{L^2},\ Rd = \frac{4\sigma^* T_c^3}{K_{bf}\beta_r},$$
$$Ha = B_0 L\sqrt{\frac{\sigma_{bf}}{\mu_{bf}}},\ Ra = \frac{g(T_h - T_c)\beta_{bf}L^3}{\alpha_{bf}\nu_{bf}}.$$

Non-dimensional initial and boundary conditions are expressed as follows:

Initial condition: $t \le 0,\ 0 \le X \le 1,\ 0 \le Y \le 1\ :\ U = V = 0,\ \theta = 0,$

Boundary conditions: $t > 0,\ 0 \le X \le 1,\ 0 \le Y \le 1\ :\ U = V = 0,$

For top wall of h-shape cavity: $\begin{cases}\theta = 0 \text{ at } Y = 0.6 \text{ for } 0 \le X \le 0.5,\\ \frac{\partial\theta}{\partial Y} = 0 \text{ at } Y = 1 \text{ for } 0.5 \le X \le 1,\end{cases}$

For bottom wall of h-shape cavity:

$$\begin{cases}\frac{\partial\theta}{\partial Y} = 0 \quad \text{at } Y = 0 \text{ for } 0 \le X \le 0.4,\\ \theta = 1 \text{ at } Y = 0.3 \text{ for } 0.4 \le X \le 0.6,\\ \frac{\partial\theta}{\partial Y} = 0 \quad \text{at } Y = 0 \text{ for } 0.6 \le X \le 1,\end{cases}$$

For bottom cut portion of h-shape cavity:

$\theta = 1$ at $X = 0.4$ & $X = 0.6$ for $0 \le Y \le 0.3$,

For right wall of h-shape cavity: $\theta = 1$ at $X = 1$ for $0 \le Y \le 1$,

For left wall of h-shape cavity: $\begin{cases}\theta = 0 \text{ at } X = 0 \text{ for } 0 \le Y \le 0.6,\\ \theta = 0 \text{ at } X = 0.5 \text{ for } 0.6 \le Y \le 1,\end{cases}$

For top wall of square cavity: $\frac{\partial\theta}{\partial Y} = 0$ at $Y = 1$ for $0 \le X \le 1$,

For bottom wall of square cavity: $\frac{\partial\theta}{\partial Y} = 0$ at $Y = 0$ for $0 \le X \le 1$,

For left wall of square cavity: $\theta = 0$, at $X = 0$ for $0 \le Y \le 1$,

For right wall of square cavity: $\theta = 1$ at $X = 1$ for $0 \le Y \le 1$,

The dimensionless form of local (Nu_L) and average (Nu) Nusselt number at the right hot wall is written as:

$$Nu_L = -\left(\frac{k_{hnf}}{k_{bf}} + \frac{4}{3}Rd\right)\left(\frac{\partial\theta}{\partial X}\right)_{X=1}, \tag{12}$$

and

$$Nu = \int_0^1 Nu_L\, dY. \tag{13}$$

3. Numerical procedure

The governing equations (1)–(4) with initial and boundary conditions are solved using the Artificial Compressibility based Finite-Difference Method (AC-FDM) with control volume and staggered grid approach. The FDM is integrated with an artificial compressibility technique to effectively compute the coupled pressure and velocity distributions in this model. Various control volume points have been utilized to ensure grid alignment with the velocity distributions. At the center of the control volume, pressure and temperature components are taken precisely. Different cell types (U-momentum, V-momentum, continuity, pressure, and temperature cells) are utilized to derive the corresponding non-dimensional equations (8)–(11). The continuity equation is adjusted using the artificial compressibility method, accounting the compressibility parameter with pressure.

The non-dimensional continuity equation is expressed as follows [46,58]:

$$\frac{1}{h}\left(\frac{\partial P}{\partial t}\right) + \frac{\partial U}{\partial X} + \frac{\partial V}{\partial Y} = 0, \tag{14}$$

where h is the artificial compressibility parameter.

Governing equations of fluid flow and energy are expressed as follows:

$$U^{n+1} = U^n + \Delta t\left[\frac{\rho_{bf}}{\rho_{hnf}}\left(-\frac{\partial P}{\partial X} + Pr\left(\frac{\mu_{hnf}}{\mu_{bf}}\right)\left(\frac{\partial^2 U}{\partial X^2} + \frac{\partial^2 U}{\partial Y^2}\right) - \frac{\mu_{hnf}}{\mu_{bf}}\frac{Pr}{Da}U\right) + \frac{\rho_{bf}}{\rho_{hnf}}\frac{\sigma_{hnf}}{\sigma_{bf}}\left(Pr\,Ha^2\sin^2\left(\frac{2\pi}{\lambda}(X\cos\psi + Y\sin\psi)\right) \times \left(V\sin\psi\cos\psi - U\sin^2\psi\right)\right) - U\frac{\partial U}{\partial X} - V\frac{\partial U}{\partial Y}\right], \tag{15}$$

Table 2
Code validation with Nardini et al. [59] results for various values of Ra with $Pr = 0.71$.

Ra	Nu [59]	Nu (Present)
5.73E + 04	3.67	3.679477200191824
1.27E + 05	4.41	4.453612543583565
1.78E + 05	4.71	4.785488901327871
2.30E + 05	5.41	5.443663504496627

$$V^{n+1} = V^n + \Delta t \left[\frac{\rho_{bf}}{\rho_{hnf}} \left(-\frac{\partial P}{\partial Y} + Pr \left(\frac{\mu_{hnf}}{\mu_{bf}} \right) \left(\frac{\partial^2 V}{\partial X^2} + \frac{\partial^2 V}{\partial Y^2} \right) - \frac{\mu_{hnf}}{\mu_{bf}} \frac{Pr}{Da} V + \frac{(\rho\beta)_{hnf}}{(\rho\beta)_{bf}} Ra\ Pr\ \theta \right) + \frac{\rho_{bf}}{\rho_{hnf}} \frac{\sigma_{hnf}}{\sigma_{bf}} \left(Pr\, Ha^2 \sin^2 \left(\frac{2\pi}{\lambda} (X \cos\psi + Y \sin\psi) \right) \times \left(U \sin\psi \cos\psi - V \cos^2\psi \right) \right) - U \frac{\partial V}{\partial X} - V \frac{\partial V}{\partial Y} \right], \tag{16}$$

$$\theta^{n+1} = \theta^n + \Delta t \left[\frac{(\rho C_p)_{bf}}{(\rho C_p)_{hnf}} \left(\left(\frac{k_{hnf}}{k_{bf}} + \frac{4}{3} Rd \right) \left(\frac{\partial^2 \theta}{\partial X^2} + \frac{\partial^2 \theta}{\partial Y^2} \right) + Q\theta \right) - U \frac{\partial \theta}{\partial X} - V \frac{\partial \theta}{\partial Y} \right]. \tag{17}$$

This iteration process is continued until the convergence of points U, V, and θ is reached at the designated time step ($\Delta t = 0.000001$). Iterative computing is carried out at each subsequent time increment until the convergence criteria is reached.

$$\frac{|\gamma_{i,j}^{n+1} - \gamma_{i,j}^{n}|}{\gamma_{i,j}^{n+1}} \leq 10^{-6} \tag{18}$$

where γ represents U, V, and θ. The grid size 91 × 91 is employed for the current numerical simulation of this study. In this study, the numerical approach employed by Basha et al. is utilized to solve the governing equations of fluid flow and heat transfer. This methodology involves a well-established numerical scheme whose accuracy and reliability have been thoroughly validated and verified in their work through benchmark studies. For detailed information regarding the numerical implementation and verification process, readers may refer to [46].

Nardini et al. [59] investigated the natural convection flow in a square cavity heated by two hot strips in the side walls. Both experimental and numerical (Fluent simulations) methods are used to analyze temperature distributions, Nusselt numbers, and flow patterns at different Rayleigh number values for varying strip positions. A comparative study is performed on average Nusselt number with the results of Nardini et al. [59] to verify the efficiency of the present numerical code at different values of Ra. Table 2 makes it clear that the current findings closely resemble the experimental findings, suggesting that the current code produces accurate results.

Grid independence test

To ensure numerical accuracy and eliminate errors associated with mesh resolution, a grid independence test was performed. The average Nusselt number was computed for both h-shape and square cavities for fixed values of pertinent parameters across progressively refined grids ranging from 51 × 51 to 101 × 101. From Table 3, it can be observed that as the grid is refined, Nu values show a monotonic convergence trend. For the square cavity, grid convergence is achieved as early as the 71 × 71 mesh size, with percentage changes below 0.05%.

Table 3
Grid independence test for h-shape and square cavities at $Q = 1$, $\phi = 0.05$, $Rd = 1$, $Da = 10^{-2}$, $Ra = 10^4$, $Ha = 25$, $\psi = \frac{\pi}{3}$, $\lambda = 0.25$, and $m = 3$.

Grid size	Nu (h-shape cavity)	Nu (square cavity)
51 × 51	2.077166	2.330125
61 × 61	2.091632	2.328838
71 × 71	2.102095	2.327969
81 × 81	2.110016	2.327347
91 × 91	2.116219	2.326881
101 × 101	2.121209	2.326519

However, for the h-shape cavity, the difference between successive grids continues to decrease gradually, dropping below 0.3% only after the 91 × 91 mesh size. Since the further refinement to 101 × 101 produces only a marginal improvement, and considerably increases the computational cost. Hence, a 91 × 91 grid was selected as the optimal mesh size. This choice ensures grid-independent results while maintaining computational efficiency.

4. Machine learning analysis

The numerical simulation data of GO–MgO–silicone oil hybrid nanofluid flow in the enclosure is utilized in this study to identify the optimal cavity shape to improve the heat transfer efficiency using machine learning techniques. By seamlessly integrating additional variables, machine learning algorithms present the multivariable models of heat transfer in a simplified way. To substantially reduce computational requirements, machine learning algorithms can adjust scales to efficiently manage various input and output features. To enhance predictive capability and model the average Nusselt number, four machine learning models (multiple linear regression, support vector machine, artificial neural network, and random forest) are trained and compared. Python is utilized to write code by using libraries like NumPy, Pandas, and Matplotlib to develop machine learning models. The statistical data of the average Nusselt number have been collected at the hot wall for different pertinent parameters, like Ha, Da, Q, Rd, Ra, and $\phi = \phi_1 + \phi_2$. This data analyzes the h-shape and square cavities, aiming to determine an ideal value for the key pertinent parameters to optimize the heat transmission rate, which is crucial in many applications: electronic cooling, building insulation, solar collectors, and industrial furnaces. A dataset of 220 values has been employed to conduct machine learning analysis. 80% of the data is used for training the model, and 20% of the data is used for testing. The performance of the four ML models is evaluated based on performance metrics (MAE, MSE, RMSE, and R^2). Based on the local minimum located through gradient descent, the cost function is utilized to optimally select the pinpoint biases and optimal weights for the present model [60].

Machine learning models

i. Multiple Linear Regression

Multiple linear regression is one of the types of supervised learning. MLR forecasts the features of the target (dependent) variable. MLR is a vital regression approach that depicts the linear relationship between several independent variables and a single continuous dependent variable. It extends ordinary least-squares regression by incorporating multiple independent variables to improve prediction accuracy. In MLR, the goal is to find the best-fitting equation that explains how the input variables (also called features or predictors) influence the output. The model assigns each variable a coefficient, representing its contribution to the prediction. These coefficients are estimated using the least squares method. The least squares method involves choosing the line (or hyperplane) that minimizes the sum of squared vertical differences between the responses and the points predicted by the

fitted line at values of the predictor variable. The major advantage of using MLR is its capability to determine the impact of one or more predictor variables on the criterion value and to understand outliers or anomalies. The model heavily depends on the assumption that the input data is accurate, complete, and relevant. Incomplete or missing data can significantly skew the results, leading to biased or unreliable predictions. In real-world situations, relationships between variables are often non-linear; linear regression performs poorly when there are non-linear relationships.

A correlation equation generated using MLR is written as follows:

Correlation equation for h-shape cavity:

$$Nu = -0.033213*Ra + 0.012888*Ha - 0.007168*Da + 0.038677*\phi - 0.088369*Q + 0.294470*Rd + 1.995950, \quad (19)$$

Correlation equation for square cavity:

$$Nu = 0.682424*Ra - 0.068516*Ha + 0.032452*Da + 0.030398*\phi - 0.150848*Q + 0.308979*Rd + 2.524462. \quad (20)$$

ii. Support Vector Machine

A support vector machine is a powerful supervised learning algorithm used for both classification and regression tasks. It works by identifying the optimal hyperplane that separates data points effectively. SVM is one of the most beneficial algorithms in detecting complex patterns in data through the use of nonlinear kernel functions. If the data is not linearly separable in its original space, a kernel function is used to implicitly map the data into a higher-dimensional feature space where separation is easier. When implementing an SVM model, users must specify the type of kernel function, which determines how input data is transformed and compared, and the regularization parameter (C), which controls the trade-off between maximizing the margin and minimizing classification errors. Common kernel functions include linear, polynomial, and Radial Basis Function (RBF). Among these, the RBF kernel is often the preferred choice for nonlinear problems due to its flexibility; it projects the data into an infinite-dimensional space. The C parameter plays a crucial role in model performance:

•A low C value enables some misclassification and results in identifying the decision boundary with a wider margin. As a result, the decision boundary is simpler and more general.

•A high C value ensures a complete as well as correct classification of the training data and yields the irregular decision boundary with a smaller margin.

In regression tasks, the SVM is known as Support Vector Regression (SVR). SVR aims to find a function $f(x_n)$ that approximates the actual target values Ω as closely as possible, while maintaining a specified tolerance ϵ. The objective is to ensure the function is both accurate and as smooth as possible, allowing for minor deviations within the ϵ-margin [61]. In this study, support vector regression with a radial basis function kernel was implemented. Key hyperparameters are penalty factor, kernel coefficient, and epsilon (ϵ), which control model complexity, margin width, and generalization capability.

iii. Artificial Neural Network

Artificial neural networks, inspired by the structure and function of the human brain, are highly effective in learning from data and predicting outcomes for unseen inputs. In recent years, the application of artificial intelligence in fluid mechanics has gained significant attention due to its strong predictive capabilities [21–23]. Motivated by this, we adopted a neural network model to predict the average Nusselt number. The network architecture consists of three hidden layers containing 128, 64, and 32 neurons, respectively. Fig. 2 illustrates the graphical representation of the neural network. Each hidden layer uses the Rectified Linear Unit (ReLU) activation function to introduce nonlinearity, enabling the model to capture complex relationships within the data. The model is trained using the Adam optimizer, which integrates the advantages of both adaptive gradient and root mean square propagation to ensure efficient and adaptive learning. The training process is conducted up to 5000 iterations, with a learning rate of 0.005, L2 regularization parameter of 0.001, and early stopping using a 15% validation split, to maintain a balance between convergence speed and stability. This configuration is designed to improve the model's accuracy and generalization capability in predicting the rate of heat transfer.

iv. Random forest regression

Random forest technique is widely recognized as a powerful and versatile ensemble learning method used for both classification and regression tasks across various fields such as healthcare, engineering, agriculture, finance, and marketing. The operational process of the random forest algorithm is depicted in Fig. 3. Random forest is built upon the principles of bagging. It is an approach where multiple models are created using the same learning algorithm but trained on different randomly sampled subsets of the training data (with replacement). The final prediction is derived by averaging the outputs of all individual models in regression problems. It incorporates the random subspace method, constructing multiple decision trees to achieve its goals. Each tree branches through a series of decision nodes until it reaches a terminal node, which generates the tree's prediction. Unlike traditional decision trees that select the best feature from all inputs when splitting the data, random forest trains each tree using a random subset of features. This approach results in each tree providing a slightly different approximation of the model, and the overall prediction is obtained by averaging the predictions of all trees [62]. One of the main advantages of the random forest algorithm is its ability to effectively handle large datasets with high dimensionality, maintaining strong performance even when the data contains noise or missing values. Averaging multiple decision trees reduces overfitting and generally achieves better accuracy and generalization than a single decision tree. Further, random forest can assess the importance of different features, which helps in feature selection and dimensionality reduction. However, random forest has some drawbacks. It can be computationally intensive, especially with very large datasets or when many trees are used, leading to longer training and prediction times as well as increased memory usage. In addition, compared to simpler models like decision trees, random forest models can be less interpretable, making it more challenging to understand the reasoning behind specific predictions. Despite these limitations, its adaptability, accuracy, and ability to handle complex datasets make it a popular choice for many practical applications [63]. In this study, a random forest regressor combining 100 decision trees via bootstrap aggregation is employed to train the model.

Model performance

Model evaluation is a way of evaluating the performance of prediction models. For regression models, evaluation metrics describe how near the prediction is to the target value. The following metrics are used in the present work [61,64]:

i. Mean Square Error (MSE)

Mean square error determines the accuracy of the model. MSE is derived from the square of the Euclidean distance. Its value is always positive, which decreases as the error tends to zero. It is defined as

$$MSE = \frac{1}{n}\sum_{i=1}^{n}\left(Nu_{Numerical(n)} - Nu_{MLR(n)}\right)^2 \quad (21)$$

where n is the data set number.

ii. Coefficient of determination (R^2)

The R^2 determines how much variation in the dependent variable is predicted by changing the independent variables. If the R^2 value is near 1, the model can predict the variance in the dependent variable.

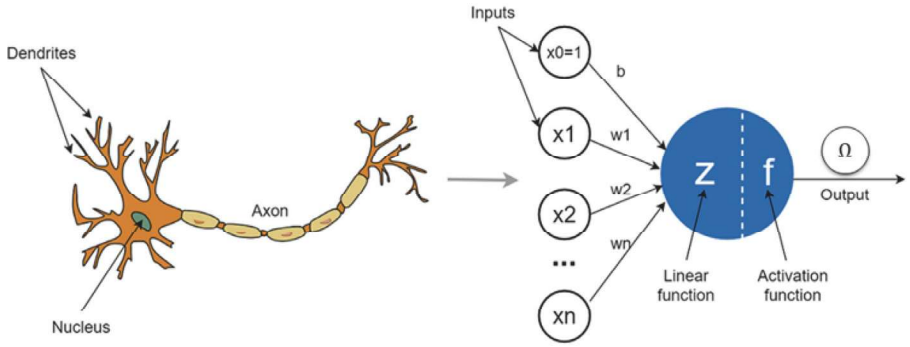

Fig. 2. Schematic diagram of an artificial neural network architecture.

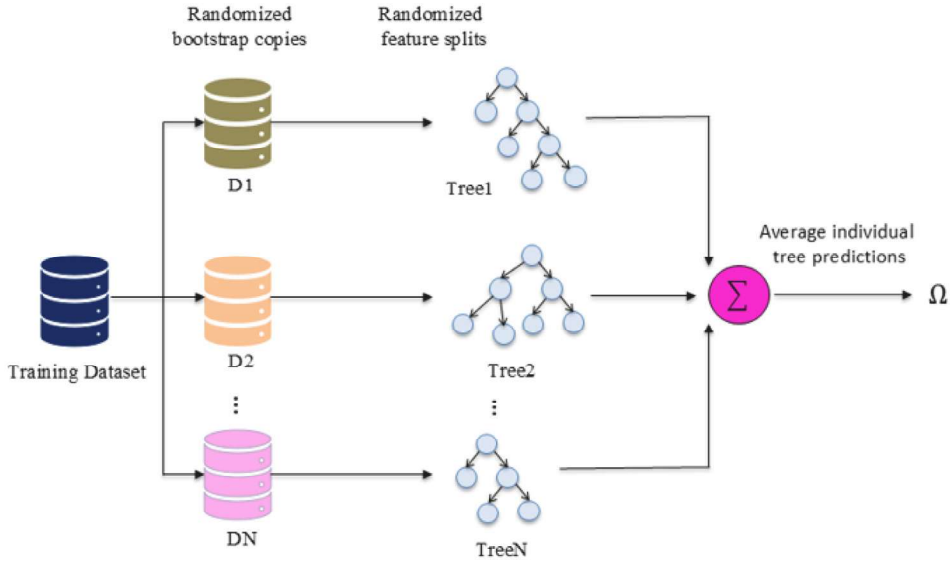

Fig. 3. Visualization of random forest learning framework.

R^2 is defined as

$$R^2 = 1 - \frac{\sum_{i=1}^{n} \left(Nu_{Numerical(n)} - Nu_{MLR(n)}\right)^2}{\sum_{i=1}^{n} \left(Nu_{Numerical(n)} - Nu_{Numerial\ mean(n)}\right)^2} \quad (22)$$

iii. Mean Absolute Error (MAE)

Mean absolute error calculates the average absolute difference between predicted and actual values. MAE gives equal weight to all errors as it uses absolute value, unlike RMSE and MSE which squares the errors, which means larger errors have disproportionately more impact. The expression for MAE is:

$$MAE = \frac{1}{n} \sum_{i=1}^{n} \left| Nu_{Numerical(n)} - Nu_{MLR(n)} \right| \quad (23)$$

iv. Root Mean Square Error (RMSE)

Root mean square error is the square root of the MSE, which measures the mean of the squared differences between actual and predicted values, then applying a square root. RMSE is often preferred over MSE because it expresses errors in the same scale as the actual values, making it more interpretable and reliable.

$$RMSE = \sqrt{MSE} = \sqrt{\frac{1}{n} \sum_{i=1}^{n} \left(Nu_{Numerical(n)} - Nu_{MLR(n)}\right)^2} \quad (24)$$

Machine learning result

Figs. 4 and 5 illustrate parameter attributes and their interactions in the h-shape and square cavities, respectively. The distribution of each feature is shown in diagonal profiles, whereas scatter profiles show the correlations between pairs of parameters. As noticed from the figures, Ra and Da attain their peak at their lower values. ϕ is fixed at 0.05 and indicates its peak at the largest value. The scatter plot shows that an increase in Rd rises Nu. In addition, Rd and Q exhibit greater influence on target values in the sample of h-shape cavity, while Ra and Rd exhibit greater influence on target values in the square cavity. Fig. 6 presents a correlation matrix heatmap that displays the pairwise Pearson correlation coefficients among the variables. This heatmap provides insight into the strength and trend of linear relationships between these variables. The range of the variables in the correlation matrix heatmap lies between −1 and 1, where 1 indicates a perfect positive correlation, 0 indicates no correlation, and −1 indicates a perfect negative correlation. When the sensitivity is positive, the output response increases while amplifying the value of the input parameters, whereas the opposite trend is observed when the sensitivity is negative. As seen in the figure, there is a strong positive correlation between Rd and Nu in the h-shape cavity and Ra and Nu in the square cavity, with a coefficient of 0.92 and 0.91, respectively. This demonstrates that the radiation parameter and Rayleigh number are the most sensitive parameters in the h-shape and square cavity,

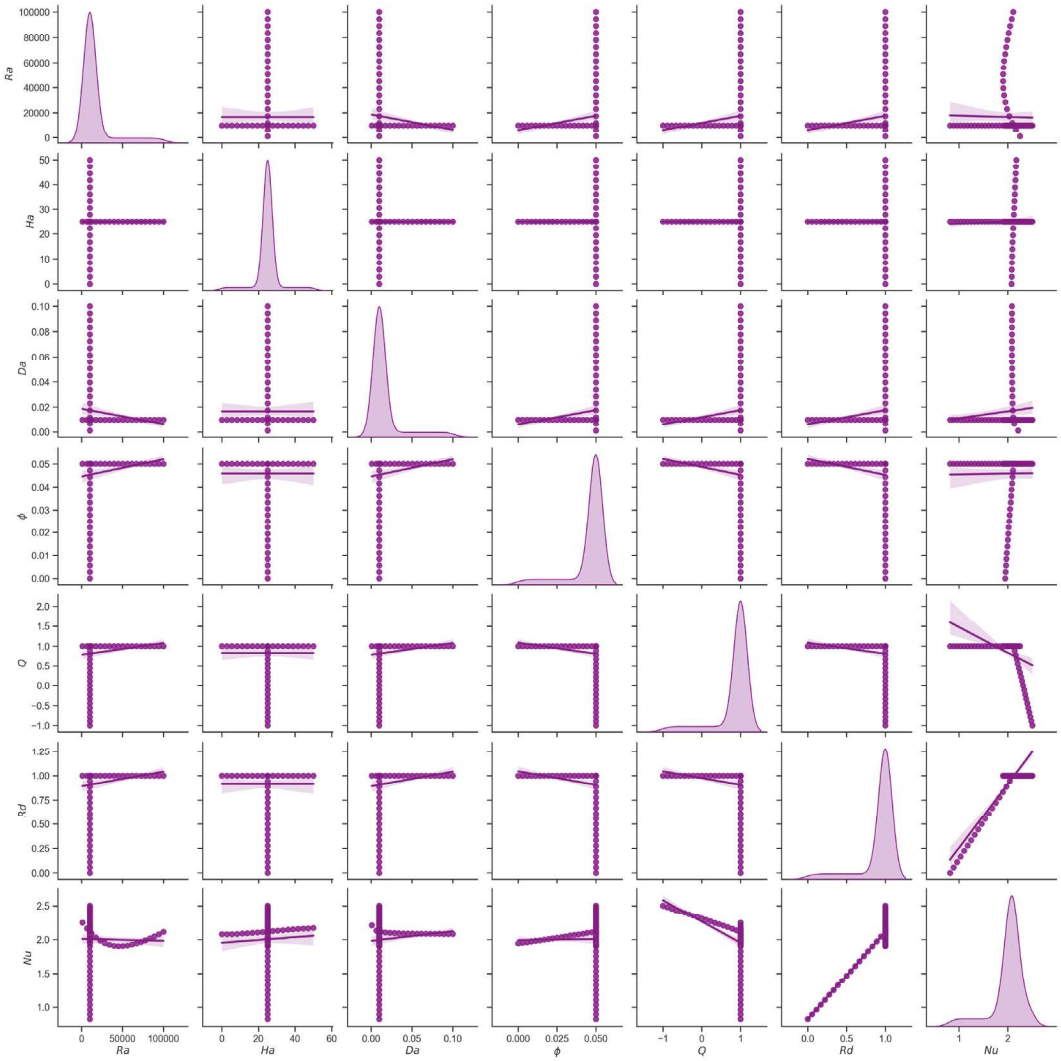

Fig. 4. Correlation of average Nusselt number with key parameters in the h-shape enclosure dataset.

Table 4
A comparison of performance metrics (R^2, MSE, RMSE, and MAE) for h-shape and square cavities.

Model	Cavity	R^2		MSE		RMSE		MAE	
		Training	Testing	Training	Testing	Training	Testing	Training	Testing
MLR	h-shape	0.9848	0.9597	0.0015	0.0034	0.0392	0.0583	0.0183	0.0318
	Square	0.9977	0.9965	0.0014	0.0032	0.0379	0.0568	0.0259	0.0382
SVM	h-shape	0.9552	0.9462	0.0045	0.0045	0.0673	0.0674	0.0589	0.0546
	Square	0.9881	0.9730	0.0075	0.0250	0.0867	0.1580	0.0634	0.0849
ANN	h-shape	0.9978	0.9925	0.0002	0.0006	0.0150	0.0252	0.0109	0.0189
	Square	0.9985	0.9965	0.0010	0.0033	0.0310	0.0571	0.0170	0.0318
RF	h-shape	0.9989	0.9904	0.0001	0.0008	0.0105	0.0284	0.0062	0.0164
	Square	0.9986	0.9891	0.0009	0.0101	0.0293	0.1003	0.0160	0.0638

respectively. The average Nusselt number is negatively sensitive to the Rayleigh number and heat source/sink parameter in the h-shape cavity, while it is negatively sensitive to the Hartmann number, Darcy number, and the heat source/sink parameter in the square cavity.

Overfitting and underfitting are major causes of concern in ML, which can be identified using several performance measures on testing and training data. The characteristics of training and testing data need to be very close to ensure that the model fits well. Table 4 presents a comparative analysis of four machine learning models (MLR, SVM, ANN, and RF) used to predict heat transfer in h-shape and square cavities. Each model is evaluated using performance metrics, the coefficient of determination, mean square error, root mean square error, and mean absolute error on both training and testing datasets. A high R^2 value (close to 1) indicates that the model explains most of the variance in the data, while lower MSE, RMSE, and MAE values suggest better prediction accuracy. The ANN and RF models demonstrate superior performance, achieving R^2 values of about 0.99 and extremely low error metrics for both cavities, with minimal difference between training and testing results. This indicates excellent generalization and model stability, without signs of overfitting. In contrast, the SVM model shows relatively higher error values and slightly lower R^2 value. Overall, the results show that the models, especially ANN and RF, effectively

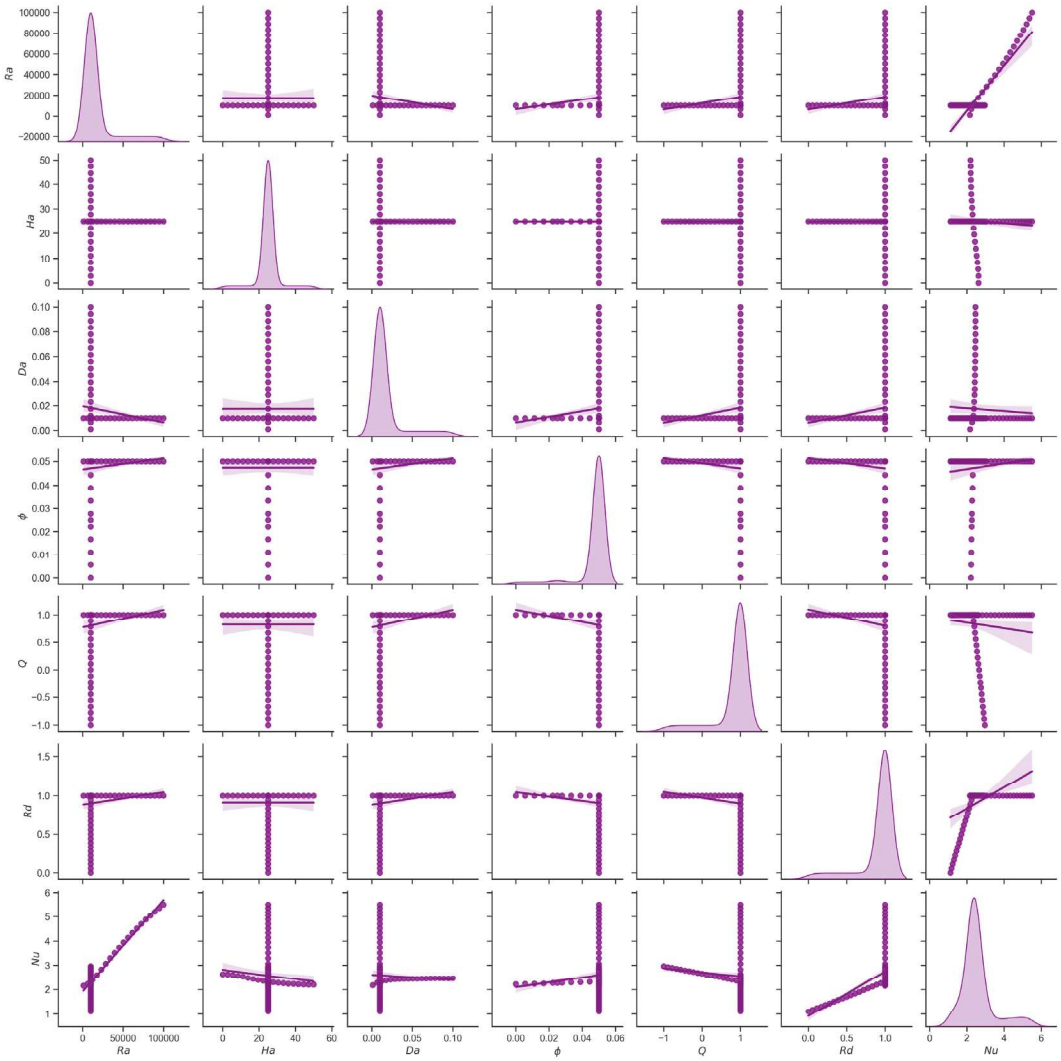

Fig. 5. Correlation of average Nusselt number with key parameters in the square enclosure dataset.

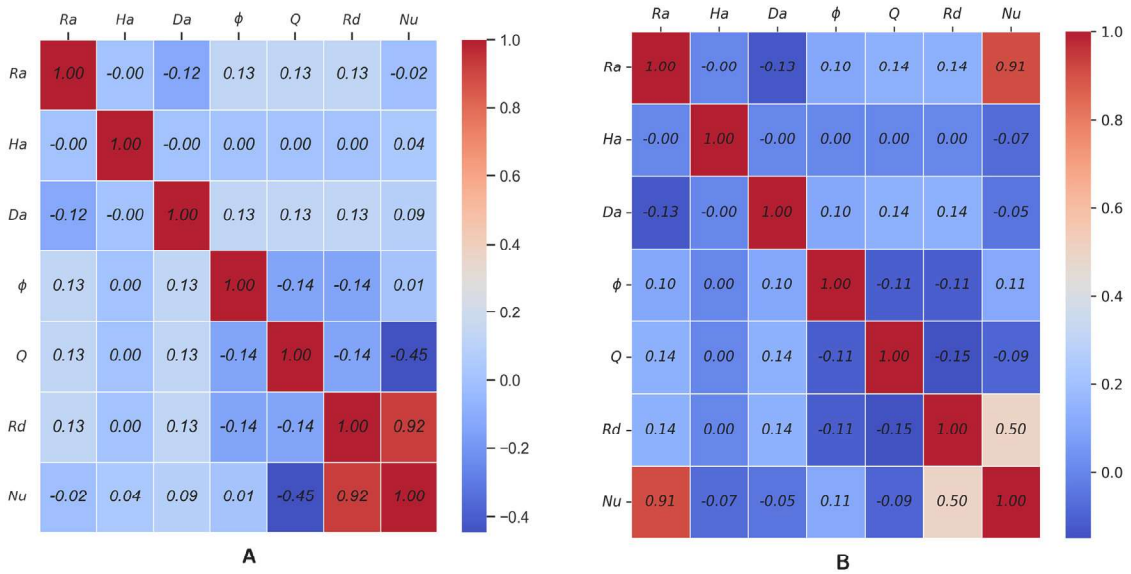

Fig. 6. Heatmap of key parameter correlations with predicted average Nusselt number in (A) h-shape and (B) square cavities.

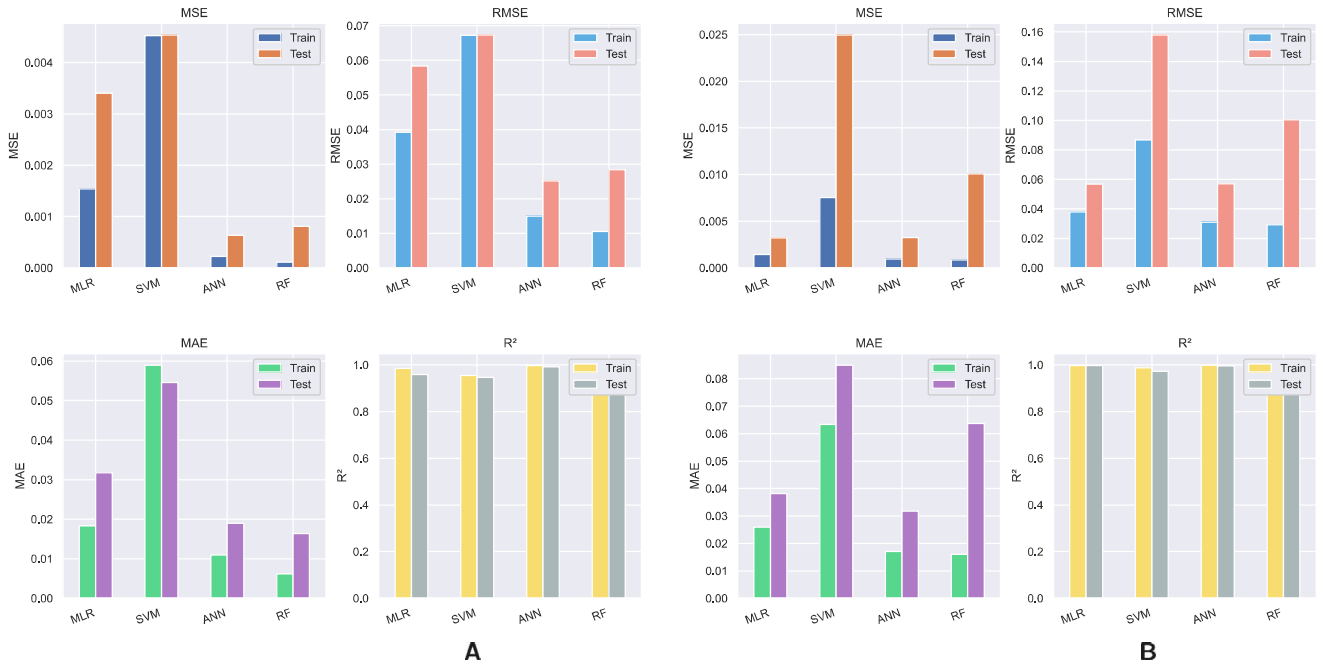

Fig. 7. Performance comparison of machine learning models in (A) h-shape and (B) square cavities.

capture the underlying physical patterns, with testing and training metrics closely aligned.

The bar charts in Fig. 7 visually illustrate the performance of four machine learning models (MLR, SVM, ANN, and RF) in predicting heat transfer characteristics for two geometries: (A) h-shape cavity and (B) square cavity. The models are evaluated using key statistical metrics: mean square error, root mean square error, mean absolute error, and coefficient of determination on both training and testing datasets. For the h-shape cavity as seen in Fig. 7(A), RF and ANN models achieve better performance, indicated by the lowest MSE, RMSE, and MAE values, as well as high R^2 values near 1, reflecting strong predictive power and minimal overfitting. SVM shows the poorest performance with high error values and the lowest R^2 value, suggesting it is unsuitable for this configuration. In the square cavity Fig. 7(B), a relatively similar pattern is observed: RF and ANN again outperform the other trained models, maintaining low error values and a high R^2 value. While MLR performs moderately, SVM exhibits significantly higher error values and underperforms in generalization. The values of the performance matrix of machine learning analysis are presented in Table 4.

Fig. 8 provides a visual representation of the prediction accuracy of various machine learning models compared to the actual average Nusselt number. The blue line represents actual value of average Nusselt number. It is noticed that RF and ANN show close alignment with the actual values, with minimal deviation across the sample range. In h-shape cavity, MLR and SVM exhibit slightly larger deviations from the actual Nu value, reflecting their lower capacity to capture nonlinear relationships between the variables. While in square cavity, MLR and SVM show comparatively better performance in predicting the average Nusselt number value. The plots clearly demonstrate that random forest and ANN provide superior predictive performance in both cavities. They effectively capture both smooth and abrupt variations in average Nusselt number, reinforcing earlier findings from the performance matrices.

Based on the comprehensive evaluation of performance matrices (MSE, RMSE, MAE, and R^2) in Table 4 and Fig. 7 and the visual comparison between actual and predicted average Nusselt number values in Fig. 8, random forest emerges as the most accurate and reliable regression model for predicting heat transfer rate in h-shape and square cavities. It consistently demonstrates the lowest error values and the highest R^2 value, indicating strong generalization and predictive performance. Therefore, considering both quantitative metrics of the table and the visual representation of figures, the random forest is selected as the optimal model for predicting heat transfer characteristics in both cavities. A comparison of the numerical values and those anticipated by the random forest is shown in Fig. 9. The performance metrics in Table 4 demonstrate that the suggested models accurately predict the heat transfer properties of hybrid nanofluid in different enclosures. The model's overall good fit efficiently handles the minor variance in forecasting even higher Nu values, as seen in this figure.

Fig. 10 illustrates error plot (I) and residual error plot (II) for the random forest model predictions in h-shape (A) and square (B) cavities. Fig. 10(I)-(A) and (I)-(B) show the error between actual and predicted average Nusselt number values, which are plotted across the considered number of samples. For both cavities, the error range approximately lies between −0.2 and 0.2. The magnitude of the error remains low, showcasing high accuracy and generalization capability of the RF model. Fig. 10(II)-(A) and (II)-(B) show the residuals against the predicted average Nusselt number. For the h-shape cavity, the residuals are tightly clustered around zero, forming a horizontal band, which suggests that the model error is consistent across the prediction range. For the square cavity, while the residuals remain mostly centered around zero, a slight spread is noticed, particularly at higher predicted values, indicating slightly increased variance but within an acceptable range.

Fig. 11 illustrates the impact of pertinent parameters on Nu in different cavity shapes using a visual pie-chart representation. The amplitudes of these characteristics are measured using RF, transformed to absolute values, and represented as percentages. Radiation parameter dominates the heat transfer, contributing 62.0219% of the total variation in Nu within h-shape cavity. Heat absorption/generation follows with 18.6124%, while nanoparticle volume fraction and Rayleigh number contribute 8.1461% and 6.9954%, respectively. Hartmann number

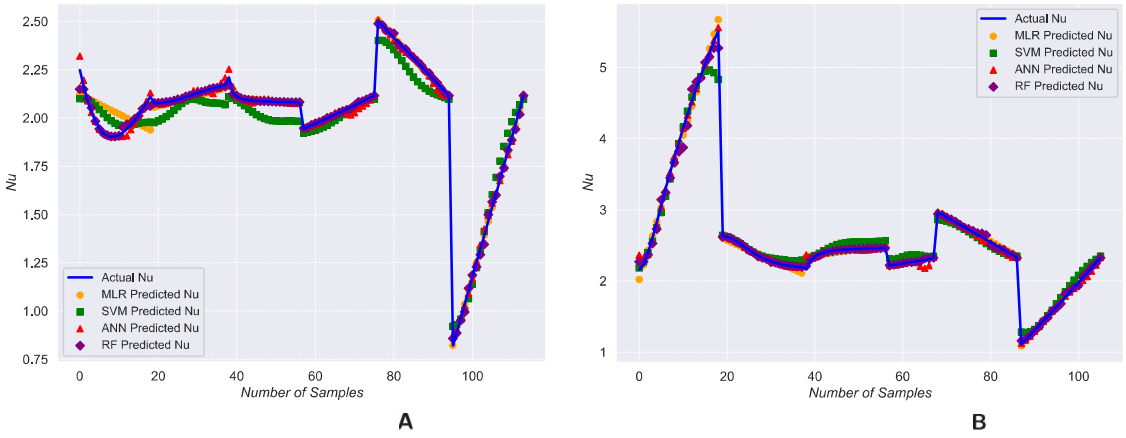

Fig. 8. Comparison of actual and predicted average Nusselt number using different machine learning models for (A) h-shape and (B) square cavities. (For interpretation of the references to color in this figure legend, the reader is referred to the web version of this article.)

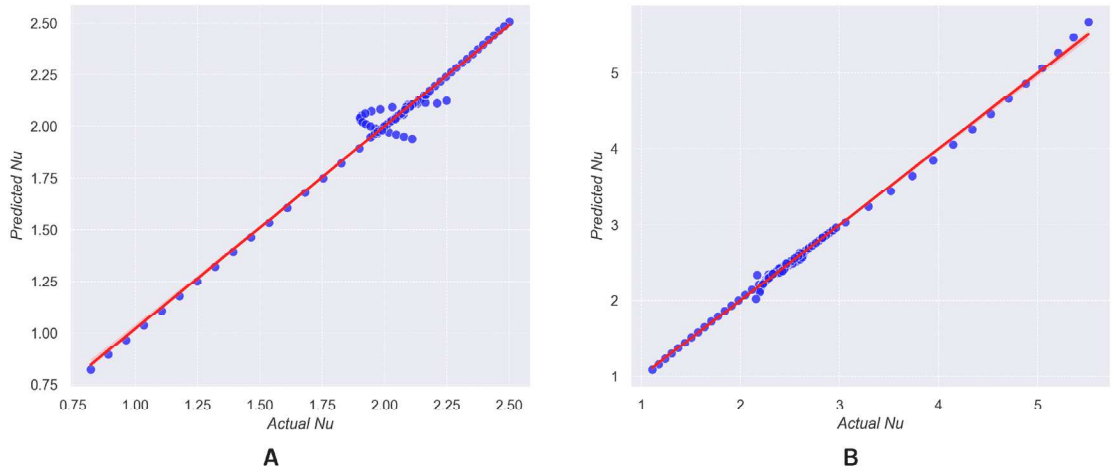

Fig. 9. Comparison of actual and predicted Nusselt number values for h-shape (A) and square (B) cavities using RF model.

and Darcy number have minimal influence, contributing only 2.7146% and 1.5097%, respectively. Where, Rayleigh number becomes the most dominant factor within the square cavity, contributing 53.5816% of the total variation in Nu, followed by radiation with 24.26%, and heat absorption/generation with 11.844%. Hartmann number, nanoparticle volume fraction, and Darcy number, have smaller contributions, 5.3796.%, 2.3868%, and 2.5480%, respectively. The outcomes demonstrate that Rd and Q have a significant impact on Nu in case of the h-shape cavity, while Ra and Rd have a significant impact on Nu in case of the square cavity. As Ra rises, the influence of the buoyancy force increases and as a result, the convective mode of heat transfer dominates, which in turn increases the Nu.

Table 5 reports the sum of squares (Sum^2), degrees of freedom (df), F-value, and p-value, for each governing parameter: Rayleigh number, Hartmann number, Darcy number, nanoparticle volume fraction, heat absorption/generation, and thermal radiation. A small p-value (<0.05) means the effect is statistically significant. The ANOVA test elucidates that the training and testing data have a high variance level, as illustrated in the table. RF effectively captures the influence of the dominant parameters, as indicated by the high F-values and extremely low p-values. From the above table, it is clear that radiation and heat source & sink parameters have a significant impact on regulating the heat transfer rate in the h-shape cavity, while Rayleigh number and radiation effects have a predominant effect in the square cavity compared with other considered effects. Among the pertinent parameters that arise from this investigation, Ra and Rd are the most influential factors in the square and h-shape enclosures, respectively.

Table 5
Statistical analysis of governing parameter for h-shape and square cavities.

Shape	Parameter	Sum^2	df	F-value	p-value
h-shape	Ra	0.131439	1.0	64.497973	1.353275×10^{-12}
	Ha	0.018382	1.0	9.020402	3.324586×10^{-3}
	Da	0.004952	1.0	2.430036	1.219831×10^{-1}
	ϕ	0.128020	1.0	62.820480	2.307794×10^{-12}
	Q	0.815957	1.0	400.396630	5.922980×10^{-38}
	Rd	8.315548	1.0	4 080.504699	4.888470×10^{-87}
Residual		0.218052	107.0	*	*
Square	Ra	51.517847	1.0	26 748.572875	$2.863883 \times 10^{-122}$
	Ha	0.416324	1.0	216.159485	1.229261×10^{-26}
	Da	0.088345	1.0	45.869562	9.109324×10^{-10}
	ϕ	0.084690	1.0	43.971714	1.773873×10^{-9}
	Q	1.784340	1.0	926.447065	4.659617×10^{-52}
	Rd	8.124748	1.0	4 218.449106	5.599594×10^{-83}
Residual		0.190674	99.0	*	*

5. Result and discussion

This study helps to optimize the cavity and nanoparticle shapes and identifies the optimum pertinent parameter values to enhance the FF and HT in the considered cavities. The hybrid nanofluid of this

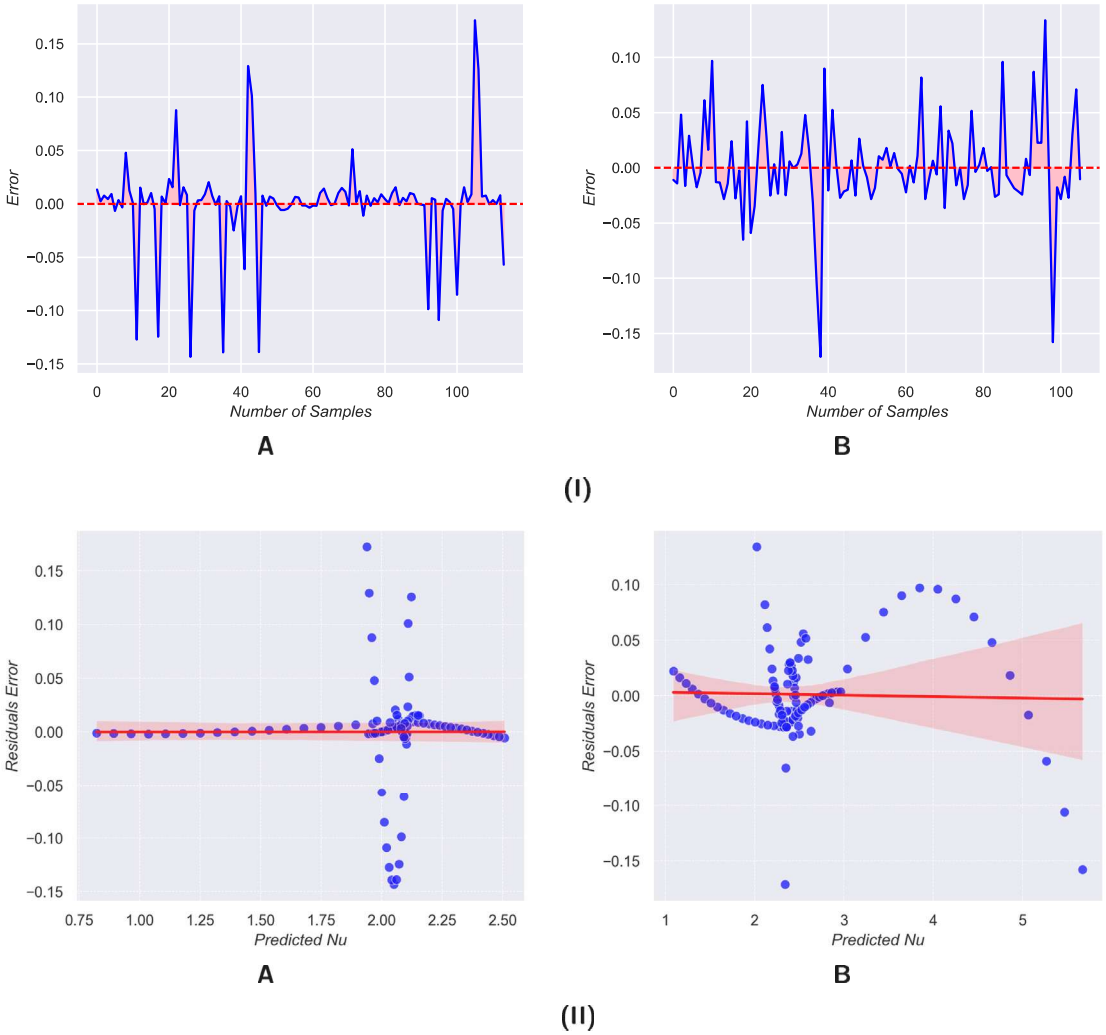

Fig. 10. Error (I) and residual error (II) between actual and predicted values for h-shape (A) and square (B) cavities.

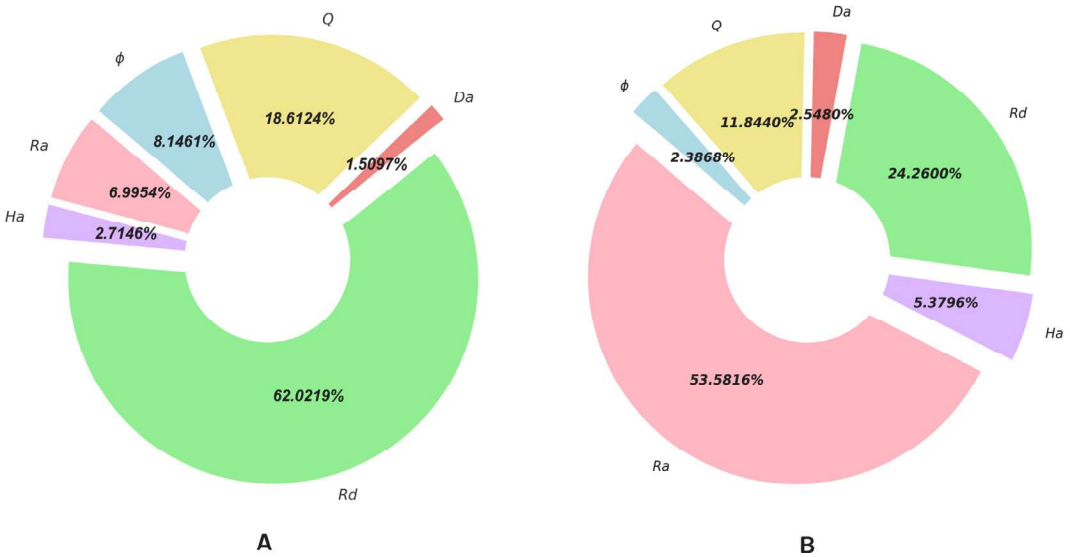

Fig. 11. Influence of pertinent parameters on the predicted average Nusselt number for (A) h-shape and (B) square cavities.

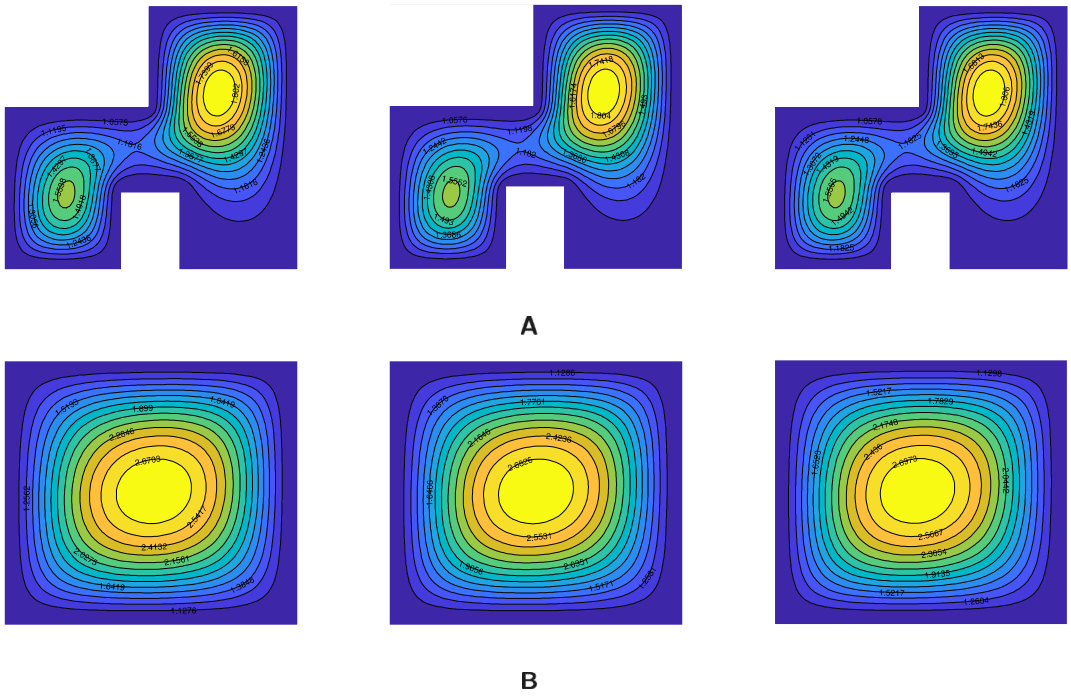

Fig. 12. Streamlines in (A) h-shape and (B) square cavities for distinct values of heat sink/source parameter (i) $Q = -1$, (ii) $Q = 0$, (iii) $Q = 1$.

study is synthesized by suspending the magnesium oxide and graphene oxide nanoparticles in the silicone oil. The computational simulation outcomes of heat transmission and hybrid nanofluid flow are shown in this section in the form of isotherms and streamlines. Average and local heat transmission rate results are discussed for the pertinent parameters. A range of governing parameters have been selected from the literature to examine the fluid flow and heat transfer characteristics of this investigation. The parameters range is fixed as follows: thermal radiation $0 \leq Rd \leq 1$, Rayleigh number $10^3 \leq Ra \leq 10^5$, heat absorption/generation coefficient $-1 \leq Q \leq 1$, Hartmann number $0 \leq Ha \leq 50$, magnetic field inclination $\frac{\pi}{6} \leq \psi \leq \frac{\pi}{3}$, Darcy number $10^{-3} \leq Da \leq 10^{-1}$, period of magnetic field $0.25 \leq \lambda \leq 0.75$, nanoparticle volume fraction $0 \leq \phi_1 + \phi_2 \leq 0.05$, and empirical shape factor $3 \leq m \leq 16.1576$. The pertinent parameter' s fixed values are: $Q = 1$, $\phi = \phi_1 + \phi_1 = 0.05$, $Rd = 1$, $Da = 10^{-2}$, $Ra = 10^4$, $Ha = 25$, $\psi = \frac{\pi}{3}$, $\lambda = 0.25$, and $m = 3$; unless otherwise specified and the Prandtl number is considered as 16.08.

Impact of heat sink/source variation on streamlines and isotherms:

Fig. 12 illustrates the influence of the heat sink/source parameter on the streamlines within two different cavities: an h-shape cavity Fig. 12(A) and a square cavity Fig. 12(B). As Q varies from -1 to 1, notable changes in fluid flow patterns are observed. A heat sink is a passive heat exchanger that transfers heat generated by a mechanical or electrical device to a coolant fluid in motion, whereas a heat source actively generates thermal energy. At $Q = -1$, corresponding to a heat sink, circulating cells are densely formed near the top-right side and the bottom-left side of the h-shape cavity. In contrast, in the square cavity, central circulation cells dominate the flow structure. As Q increases to 0, indicating the absence of heat generation or absorption, the size and intensity of the eddies slightly increase in both cavities. At $Q = 1$, representing a heat source, the circulation becomes slightly more. The enhanced thermal energy leads to increase fluid velocity as Q increases. Notably, the square cavity exhibits higher flow intensities and fluid velocities compared to the h-shape cavity for all values of Q. This indicates that the square cavity facilitates stronger convective flow under similar thermal conditions.

Isotherm contours are useful indicators for assessing the efficiency of heat transmission in fluid flow. Fig. 13(A) and (B) present the influence of the heat source/sink parameter on isotherms within h-shape and square cavities, respectively. The h-shape cavity exhibits a slightly higher magnitude compared to the square cavity. As the value of Q increases, it has a slight effect on the isotherm distribution in both the cavities, indicating a slight enhancement in convective heat transfer. The region of higher magnitude isotherms is slightly extended, indicating heat is transferring from the hot to the cold wall. Further noticed that in the square cavity a curvy pattern of isotherms is observed, indicating intensified convective heat transfer. This suggests that convection plays a more dominant role in heat transfer within the square cavity as Q increases.

Impact of Darcy number variation on streamlines and isotherms:

Darcy number value is directly proportional to the permeability of a porous medium; thus, a lower Darcy number signifies a porous medium with lower permeability. As permeability increases, fluid flows more easily through the medium, enhancing fluid flow within the porous domain. The volume of fluid infiltration and flow in the porous domain is determined by viscous resistance and inertial forces. When porous medium permeability is at a low level (i.e., $Da = 10^{-3}$), viscous resistance dominates over inertial force, significantly impeding fluid flow. However, as the permeability of the porous medium increases, the influence of inertial forces becomes more prominent, reducing the effect of viscous resistance. Consequently, fluid flow within the porous medium increases with increasing Darcy numbers. Fig. 14(A) illustrates the effect of the Darcy number on fluid flow within the h-shape cavity. At Darcy number $Da = 10^{-3}$, circulation cells are densely formed near the top-right and bottom-left sides of the cavity. As the Darcy number increases to $Da = 10^{-2}$, the strength of the circulation cells magnifies significantly. For a higher value of $Da = 10^{-1}$, the circulation cells exhibit a high magnification in magnitude, which represents a more pronounced flow that develops inside the cavity. Fig. 14(B) depicts the transport characteristics of nanofluid flow in the square cavity. A central circulating flow pattern, with the vortex core located at the cavity's center, is observed in the square cavity. As the Darcy number increases, the magnitude of the circulation cells increases. Notably, the

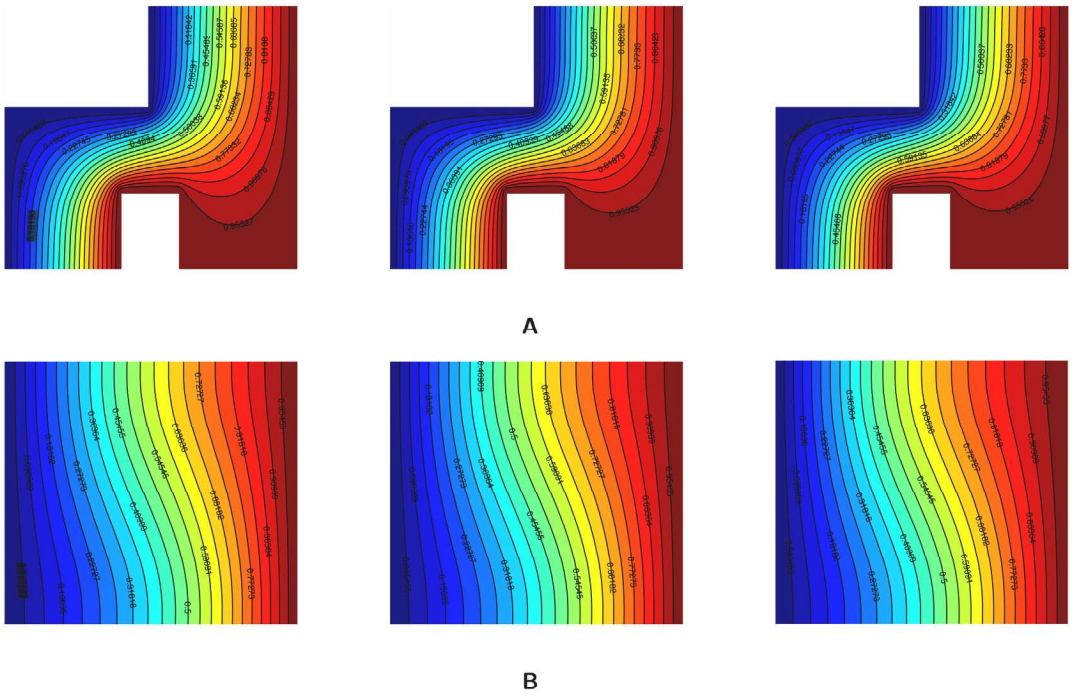

Fig. 13. Isotherms in (A) h-shape and (B) square cavities for distinct values of heat sink/source parameter (i) $Q = -1$, (ii) $Q = 0$, (iii) $Q = 1$.

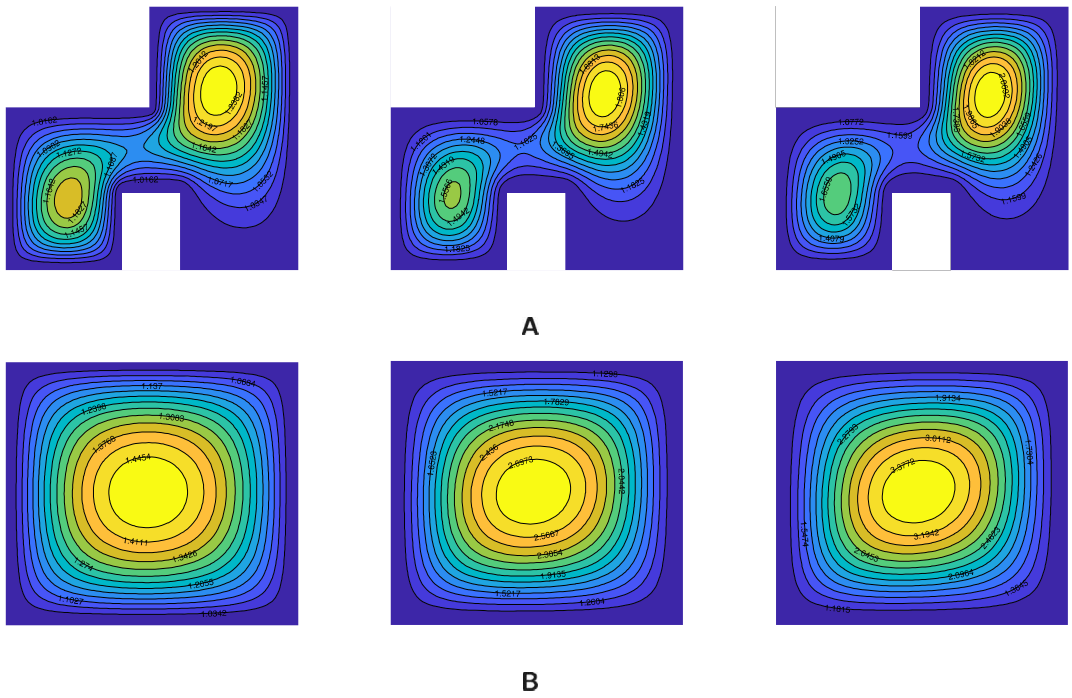

Fig. 14. Streamlines in (A) h-shape and (B) square cavities for distinct values of Darcy number (i) $Da = 10^{-3}$, (ii) $Da = 10^{-2}$, (iii) $Da = 10^{-1}$.

fluid flow is stronger in the square cavity compared to the h-shaped cavity, as seen through the high magnitude value of the streamlines of the square cavity.

Fig. 15(A) and (B) illustrate the isotherms for various values of Darcy number within h-shape and square shape cavity respectively. The isotherms provide insight into the effective heat transfer features, hence playing an important role in examining the thermal performance of nanofluids. In the h-shape cavity, increasing the Darcy number does not lead to any significant changes in the isotherm patterns and magnitude, indicating limited enhancement in heat transfer. In contrast, the square cavity exhibits a considerable variation in heat transfer features inside the cavity. As the Darcy number increases from $Da = 10^{-3}$ to $Da = 10^{-1}$, the heat transfer becomes dominant inside the cavity as seen through the curvy isotherm profiles. The curvy outline of the isotherms indicates the pathways of heat flow, illustrating the HT impact in those areas. These results are consistent with previous studies [57].

Impact of Hartmann number variation on streamlines and isotherms:

The Hartmann number defines the ratio of magnetic to viscous forces in magnetohydrodynamic flows. As the strength of the applied

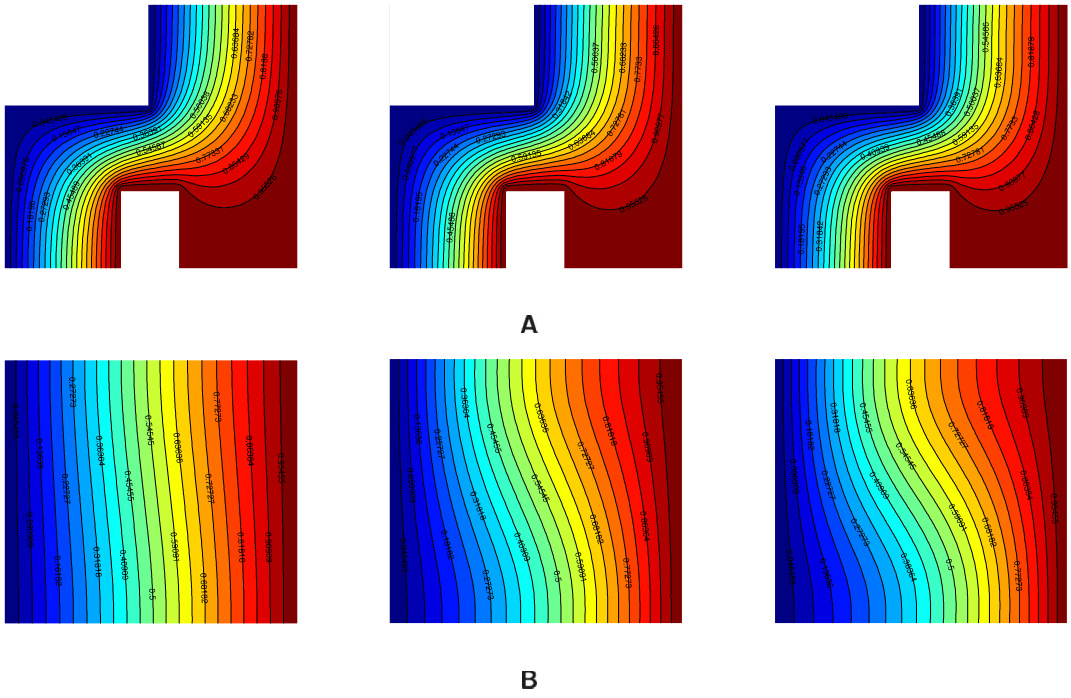

Fig. 15. Isotherms in (A) h-shape and (B) square cavities for distinct values of Darcy number (i) $Da = 10^{-3}$, (ii) $Da = 10^{-2}$, (iii) $Da = 10^{-1}$.

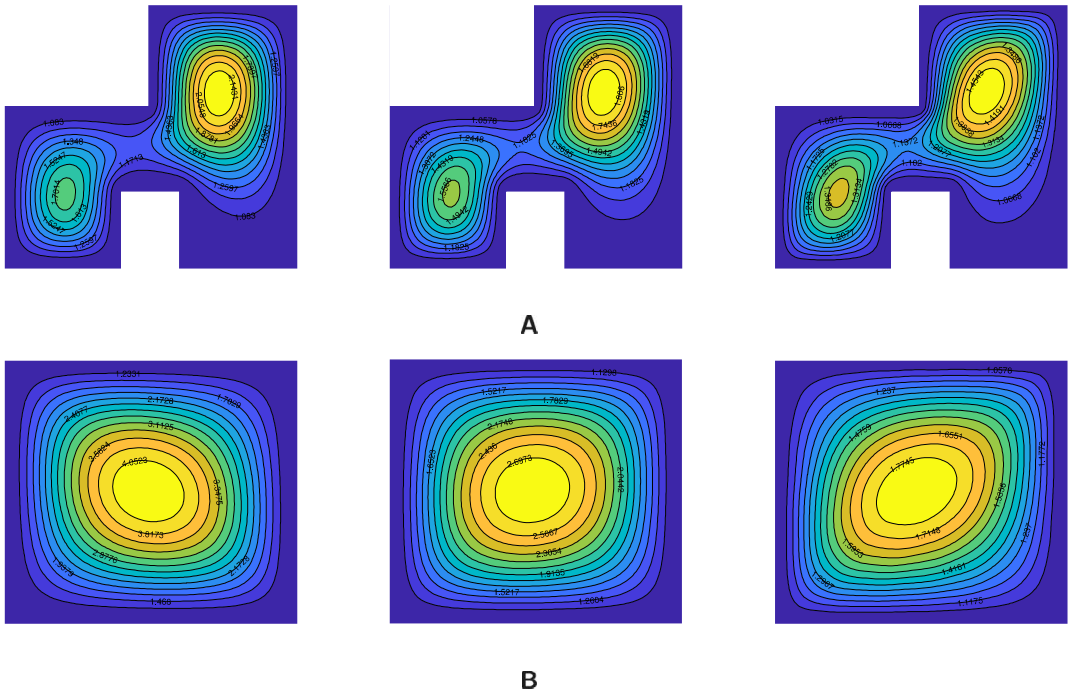

Fig. 16. Streamlines in (A) h-shape and (B) square cavities for distinct values of Hartmann number (i) $Ha = 0$, (ii) $Ha = 25$, (iii) $Ha = 50$.

magnetic field increases, the fluid velocity decreases in the cavity, which is reflected by the diminished magnitude of eddies. This reduction in flow velocity is due to the intensified effect of the Lorentz force. The Lorentz force arises from the interaction between the magnetic field and the motion of the electrically conductive nanofluid. These results are consistent with previous studies [57]. In the h-shape cavity, as shown in Fig. 16(A), as Ha increases, the circulation cells extend toward the center of the cavity, while the magnitude of the streamlines diminishes. This trend highlights the suppressing effect of the magnetic field on fluid motion. Fig. 16(B) illustrates the streamlines for the square cavity. A dominant vortex forms at the cavity's center, with circulation sensitivity localized at the center of the cavity. At $Ha = 0$, the vortex exhibits a slight inclination toward the bottom-right corner of the cavity. As Ha increases to 25, there is no inclination in the circulating cells of the cavity. For $Ha = 50$, the vortex is slightly inclined toward the bottom-left corner of the cavity. Compared to the h-shape cavity, the square cavity demonstrates higher fluid velocity in the cavity for all the values of Ha. Further, compared to the h-shape cavity, the impact of magnetic field is predominantly elucidated in the

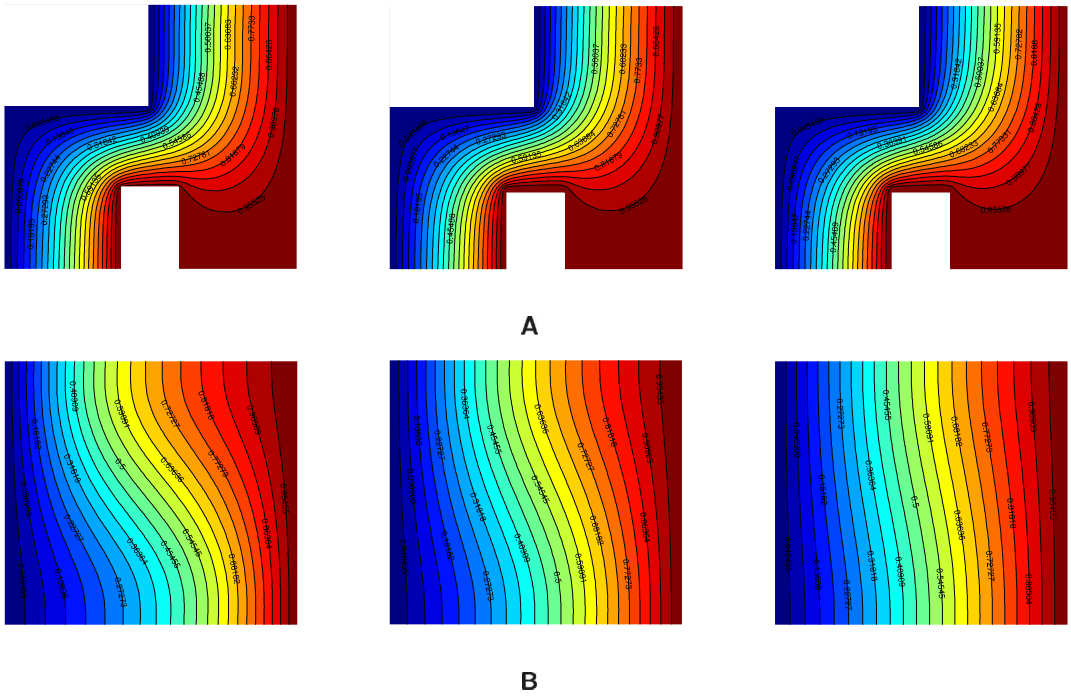

Fig. 17. Isotherms in (A) h-shape and (B) square cavities for distinct values of Hartmann number (i) $Ha = 0$, (ii) $Ha = 25$, (iii) $Ha = 50$.

square cavity, which is noticed through the strong deduction in the magnitudes of streamlines.

Fig. 17(A) and (B) illustrate the isotherms for varying Hartmann numbers, showing the influence of magnetic field strength on heat transfer characteristics. In the h-shape cavity, there is no significant difference in the isotherms by varying the value of Ha. Conversely, in the square cavity, the nature of heat transfer varies considerably as Ha increases; the curviness of the isotherms in the top-right corner reduces. This is due to the impact of the Lorentz force, which arises when charged particles in the electrically conductive fluid travel through magnetic and electric fields. This force acts to slow down fluid motion, and thereby the heat transfer nature within the enclosure is affected.

Impact of Rayleigh number variation on streamlines and isotherms:

The Rayleigh number is defined as the ratio of inertia force to viscous force, influenced by various factors, including fluid velocity fluctuations, and characterizes the strength of natural convection in the fluid flow. The impact of Ra on streamlines is elucidated in Fig. 18(A) and (B) for h-shape and square cavities, respectively. With increasing Ra, the magnitude of streamlines increases in both the cavities due to enhanced buoyancy-driven flow, and the rotational strength of the circulating cells increases accordingly. In the square cavity, a dominant central vortex is observed across all values of Rayleigh number, and circulation sensitivity is located at the center of the cavity. At $Ra = 10^3$, this vortex shows a slight inclination toward the bottom-left corner. As Ra increases to 10^4, the inclination disappears. At $Ra = 10^5$, the size of the innermost circulating cell enlarged, and the vortex inclined toward the bottom-right wall of the enclosure.

Fig. 19(A) and (B) in order, represent the isotherms for varying Rayleigh numbers $10^3 \leq Ra \leq 10^5$ for h-shape and square cavities. At $Ra = 10^3$, conduction dominates as the primary mode of heat transfer. There is no significant change in the magnitude of isotherms in both cavities while increasing the Rayleigh number. As Ra varying from 10^3 to 10^4, there is minimal change in the isotherm patterns for h-shape cavity, while in the square cavity, isotherms start forming a curvy pattern, showing that the convective mode of heat transfer effect magnifies. A significant enhancement in heat transfer is observed when the Rayleigh number increases from 10^4 to 10^5. This is due to the growing influence of buoyancy-driven convection, which becomes increasingly dominant at higher values of Rayleigh number, leading to stronger thermal gradients and more pronounced convective heat transfer is noticed in square cavity. For nanoparticles of spherical and non-spherical shapes, Table 6 demonstrates the outcomes of average Nusselt number in h-shape and square cavities. Comparative percentage increase of average Nusselt number are presented in three forms in the table: variation with shape factor (I), variation with cavity shape (II), and variation between spherical and non-spherical nanoparticles (III). The results show that non-spherical nanoparticles consistently enhance heat transfer performance. It is noticed that Nu increases progressively as the shape factor rises. Square cavity exhibits higher heat transfer than h-shape cavity for all nanoparticle shapes, although the relative improvement decreases slightly for larger values of shape factor. Further, highest average Nusselt numbers are achieved when lamina-shaped nanoparticles are suspended in the base fluid. In contrast, spherical shape nanoparticles yield the lowest Nu in both the cavities. Among all configurations, the square cavity containing lamina-shaped nanoparticles exhibits the most efficient heat transfer performance, while the h-shape cavity with spherical nanoparticles provides the lowest heat transfer rate. Overall, both cavity shape and nanoparticle shape exert a strong influence on heat transfer rate. Fig. 20 illustrates the variation of the average Nusselt number for the h-shape and square cavities for different period of MF. The results demonstrate that λ plays a minute role in enhancing the average heat transfer rate. The percentage increase in Nu for each cavity shape is depicted in the figure. For $\lambda = 0.25$, $\lambda = 0.5$, and $\lambda = 0.75$, average Nusselt numbers for the h-shape cavity is 2.115714, 2.117939, and 2.117686, and for the square cavity it is 2.326881, 2.327504, and 2.329404, respectively. These values confirm that the square cavity consistently exhibits higher heat transfer performance. This result is consistent with the results of [32]. The influence of thermal radiation on the average Nusselt number Nu for h-shape and square cavities is illustrated in Fig. 21. As the radiation parameter increases, the rate of heat transfer is significantly enhanced. This is due to the contribution of radiative heat transfer, which becomes increasingly dominant at higher values of Rd. In this figure, the percentage of increase in Nu for the h-shape and

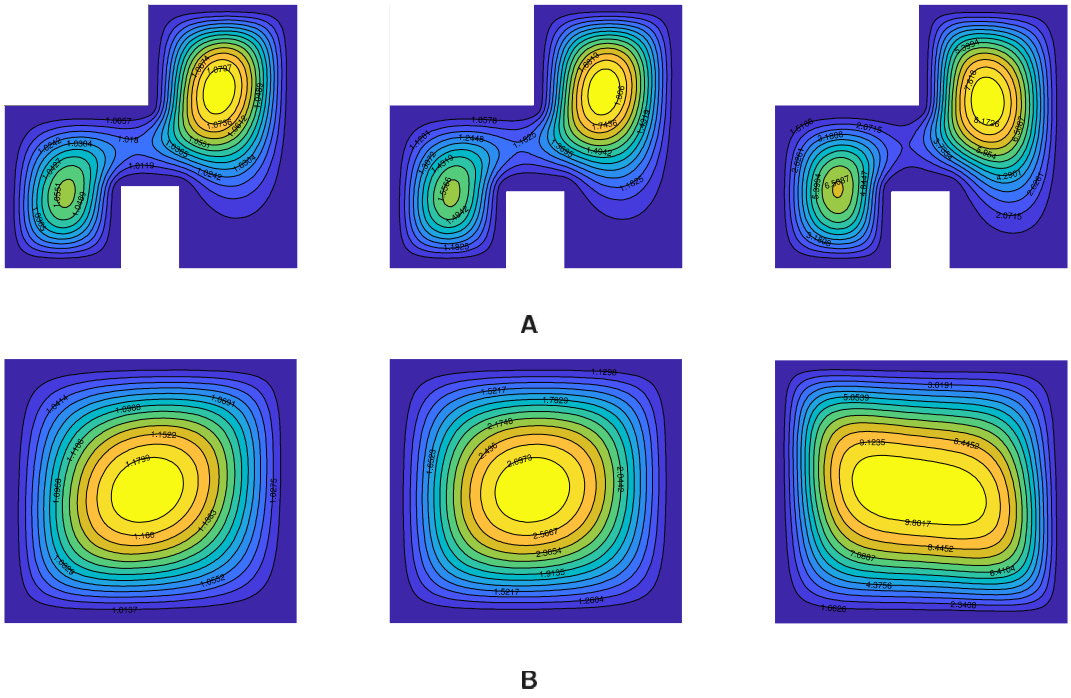

Fig. 18. Streamlines in (A) h-shape and (B) square cavities for distinct values of Rayleigh number (i) $Ra = 10^3$, (ii) $Ra = 10^4$, (iii) $Ra = 10^5$.

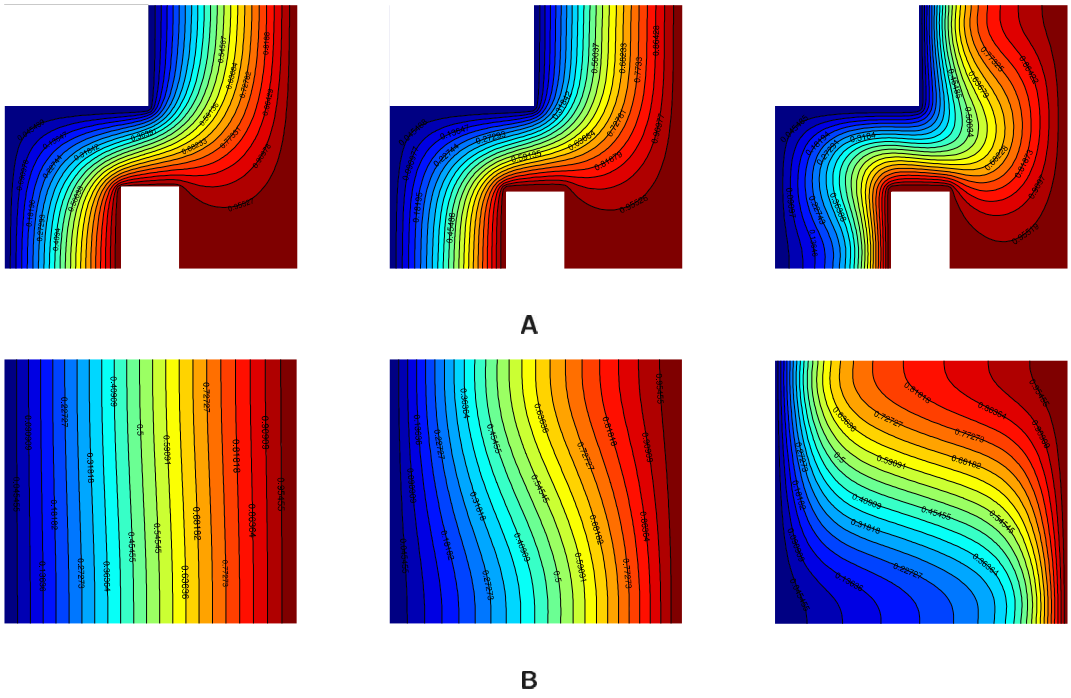

Fig. 19. Isotherms in (A) h-shape and (B) square cavities for distinct values of Rayleigh number (i) $Ra = 10^3$, (ii) $Ra = 10^4$, (iii) $Ra = 10^5$.

square cavities are illustrated. For $Rd = 0$, $Rd = 0.5$ and $Rd = 1$, average Nusselt number for the h-shape cavity is 0.821149, 1.46473, and 2.115714, and for the square cavity, it is 1.111755, 1.706436, and 2.326881, respectively. These results indicate that the square cavity consistently yields higher heat transfer rates compared to the h-shape cavity. However, both geometries exhibit a strong positive correlation between the radiation parameter and heat transfer rate, demonstrating the amplifying effect of thermal radiation on heat transfer rate within the enclosures. These results are consistent with previous studies [57].

Table 7 illustrates the effect of the Rayleigh number on the average Nusselt number Nu for the h-shape and square cavities. It is noticed that for the h-shape cavity, the average heat transfer slightly decreases as Ra increases, dropping from 2.248158 at $Ra = 1000$ to 1.901541 at $Ra = 45\,000$. However, beyond this value of Ra, the heat transfer starts to increase slightly as Ra rises, reaching 2.11058 at Ra = 100 000. This behavior is consistent with observations reported in the literature [65], where geometric complexity can lead to localized flow recirculation and unstable convection patterns at moderate buoyancy forces. Conversely, in the square cavity, Nu increases steadily with rising Ra,